Molecular-dynamics study of the reconstructed Au(111) surface: Low temperature

Ramon Ravelo and M. El-Batanouny
Department of Physics, Boston University, 590 Commonwealth Avenue, Boston, Massachusetts 02215
(Received 8 June 1989)

We study the stability and dynamics on the reconstructed Au(111) surface using three-dimensional molecular-dynamics simulations. The small-amplitude surface-phonon dispersions are calculated along the ⟨110⟩ direction and compared with inelastic-He-scattering data. The agreement with the experimental data is remarkable, given that the parameters of the surface interatomic potentials are chosen solely to reproduce the size and type of the observed surface dislocations. Low-lying localized modes (soliton modes) appear in all three polarizations and localized modes with polarization in the sagittal plane are observed around the K point with energies of about 8 meV.

I. INTRODUCTION

It has been amply demonstrated over the past two decades that the structure of clean surfaces usually deviates from that of the bulk. The deviation is identified as either a relaxation or reconstruction depending on whether it involves changes in the interlayer distances near the surface or it incorporates a deviation of the structure and geometry of the surface layer itself from the bulk morphology. Extensive studies of various systems exhibiting such deviations have been reported in the literature and were predominantly measured by low-energy electron diffraction (LEED).[1,2] Among the systems studied are the close-packed (111) surfaces of fcc metals. Although quite a few such surfaces involved some degree of relaxation, gold was found to be the only metal in this group that exhibits the phenomenon of reconstruction of the (111) surface.[2,3]

Recent application of helium-atom scattering[4] (HAS) and transmission electron microscopy[5-7] (TEM) to the study of the gold (111) reconstruction have confirmed that the reconstructed unit cell has a periodicity of $(22\pm1)\times\sqrt{3}$. Furthermore, a TEM (Ref. 7) result suggested that the reconstruction involves an ordered array of boundaries between surface regions of ABC and ABA stacking. HAS,[4] with a high degree of spatial resolution and surface sensitivity to allow the detection of surface corrugation of about 0.02 Å, was able to provide a more detailed picture of the reconstruction: on the one hand, it furnished information about the shape of the boundaries suggesting that they can be modeled by sine-Gordon (SG) solitonlike profiles, and thus a SG soliton lattice, and, on the other hand, showed that the width of the regions with ABA stacking are not equal to those with ABC stacking. Since a SG soliton lattice is characterized by equally spaced SG solitons, belonging to the class of connoidal solutions to the sine-Gordon equation,[8] the second observation posed an apparent contradiction. This problem was resolved by the introduction of the double-sine-Gordon (DSG) soliton model[9] which, in effect, incorporates a lattice of bound pairs of SG solitons. The proposed DSG model allows for the coexistence of ABC and ABA stacking with different domain widths with the ABA-stacked domain being located between the bound-soliton pair (which hereafter will be referred to as subsolitons). Recent scanning-tunneling-microscopy (STM) experiments[10] provided a detailed picture of the real-space atomic arrangement in the reconstructed surface which corroborated the picture obtained from the DSG model. Moreover, an accurate measure of the size of ABA stacking regions relative to ABC stacking regions can be easily extracted from these results, giving a ratio of 0.50.

The significance of the DSG model goes beyond just being a convenient picture of the surface structure. In fact, it provides a framework within which a clear and straightforward connection between the details of the observed structural features and the underlying energetics that produces them. Consequently, it has the unique power of establishing a model Hamiltonian based on definite relationships between the structural length scales of the soliton lattice and the energy parameters that enter into it. In turn, the established Hamiltonian can be used to study the dynamical properties of the associated system, namely, the reconstructed Au(111) surface. It is one of the main goals of this work to demonstrate the potential of such a model.

In the past five years the experimental study of surface phonons of transition and noble metals has been conducted by means of high-resolution He-atom spectroscopy[11] (HRHAS) and high-resolution electron-energy-loss spectroscopy (HREELS).[12] Recent HRHAS (Ref. 13) experiments have revealed some unusual features in the surface dispersion curves of noble metals: Cu(111) and Ag(111) show, in addition to the Rayleigh mode, an anomalously soft resonance that was not predicted in all previously published lattice-dynamical (LD) calculations based on force constants determined from a best fit of bulk dispersion curves.[14,15] Since the Ag(111) surface was known not to reconstruct, the new mode was attributed to a "peeling off" of a mode from the longitudinal bulk band edge analogous to the well-studied "peeling off" of the

 ©1989 The American Physical Society

Rayleigh mode from the transverse bulk edge produced by the boundary conditions at the surface. As in the Rayleigh mode, the vibrational amplitude at the surface is expected to increase with increasing shift in frequency. Bortolani *et al.*,[16] working within the framework of a force-constant LD slab model, have proposed an *ad hoc* softening of the in-plane surface force constants as a possible source of the anomaly. This was more directly supported by extensive comparison between calculated and experimental time-of-flight (TOF) spectra.[17,18] Several speculations as to the origin of this softening has been reported and all seem to focus on the role of the *sp* electronic states. Bortolani[16] has attributed the softening to a weakening of *s*-*d* hybridization. The presence of hybridization usually enhances the *d* occupation, and for nearly full *d* bands it tends to increase the short-range repulsion between neighboring *d* shells. The presence of the surface-vacuum interface reduces the hybridization and tends to decrease the *d*-*d* repulsion from its nominal value in the bulk. The decrease in repulsion is thus reflected in the reduction of the in-plane surface force constants. Heine and Marks[19] discussed a similar model for the noble metals. However, this picture incorporates more subtle competition between a pairwise *d*-*d* repulsive potential and a multiatom *sp*-like electron-gas attraction. The attractive forces are attributed to an anomalously deep attractive mantle in the pseudopotential. Jayanthi *et al.*[20] proposed that the contribution of the *sp* charge to the observed phonon anomalies can be treated by including a multipole expansion of the *sp* charge in a phenomenological LD slab model. The multipole expansion is taken around a high-symmetry point in the interstitial regions where the *sp* charge density is highest. In such a description the electronic degrees of freedom are treated as fluctuating multipole moments whose coupling to the ion displacements produces the desired softening. The model reproduces the observed surface phonon dispersions of Cu(111) and Ag(111) including the anomalous softening.

The case of Au(111) represents an extreme example of the reduction of surface force constants, where the surface goes through an instability that drives the reconstruction. The experimental measurements of the phonon dispersions of the reconstructed Au(111) surface show what appears to be two soft surface-acoustic branches, which lie far below the transverse bulk edge.[13] Furthermore, the lower branch seems to terminate at about the middle of the surface Brillouin zone (SBZ). The model of Jayanthi *et al.*,[20] although able to reproduce correctly the softening in Cu and Ag, could not reproduce the large softening observed in the Au(111) surface modes. However, it predicts a lattice instability at long wavelengths where unstable surface-phonon modes appear in their calculated dispersion curves around the $\bar{\Gamma}$ point for the unreconstructed Au(111) surface. Santoro *et al.*[21] attempted to improve upon the Bortolani model by performing LD slab calculations for both *ABC* and *ABA* stacking in order to investigate the effects of the reconstruction on the experimental phonon inelastic scattering intensities. Although the above-mentioned models provided reasonable agreement in fitting the experimental dispersion curves of Cu(111) and Ag(111) and explaining the observed anomalies, they fell short of achieving similar success in fitting the measured Au(111) data and in providing a convincing explanation for the rather abrupt termination of the lower surface-phonon branch. We believe that the shortfall of all these models is that they ignore, first, the dynamic role of the dislocations in modifying the dispersion curves, and second, the effect that the lowering of the symmetry of the reconstructed surface, from that of the unreconstructed one, has on removing existing degeneracies of the phonon branches specially at the boundary of the SBZ.

The present work tries to remedy these shortfalls by investigating the actual reconstructed surface using a molecular-dynamics (MD) approach. Tossati and coworkers[22–25] carried out extensive MD simulations of Au surfaces, including the (111) surface. Their work on Au(111) includes investigation of the energetics and static configuration of the reconstruction at $T=0$ as well as the surface melting behavior employing an empirical parametric many-body–force model that is able to reproduce a large variety of bulk properties. In their model the optimal size of the reconstruction cell turns out to be $11\times\sqrt{3}$ (Ref. 24) which is about half the size of the actual reconstructed unit cell. We attribute their difficulty in reproducing the right reconstructed unit cell with the short range of the ionic potential used in their model which is thus unable to discriminate energetically between *ABC* or *ABA* stacking. This, as we will see is crucial in order to incorporate DSG dislocations in the reconstruction. In this work, the DSG model is employed to establish a fundamental connection between the measured length scales characterizing the dislocations and their periodicity and the energy scales of the parameters that appear in the interatomic potentials. We make use of an effective Hamiltonian in which the surface-surface, surface-bulk, and bulk-bulk interactions are described by three pairwise potentials. The role of the *sp* electrons is incorporated by introducing a mismatch between the unstrained surface periodicity and the bulk periodicity. This is accomplished by making the surface-surface forces attractive at the bulk equilibrium atomic radius R_B^0. This creates a competition between the surface-surface and surface-bulk interactions. The creation of dislocations may be viewed as a compromise between having the surface atoms reduce their equilibrium atomic spacing or occupying the minimum-energy sites of the effective substrate potential. The spontaneous creation of dislocations depends on the value of the misfit relative to the ratio of the strengths of the surface-surface interaction to the surface-bulk interaction.[26] A critical misfit can be defined, below which the reconstructed state is stable relative to the unreconstructed state. Frank and van der Merwe[26] worked out the equilibrium conditions for the one-dimensional DSG chain with free ends. Okwamoto and Bennemann[27] arrived at conditions for the critical misfit of the Au(111) surface as a function of surface shear and bulk modulus working in a two-dimensional continuum model. Their model, however, assumed that at the surface the *A* and *C* sites are energetically degenerate and thus, it is only able to reproduce

sine-Gordon dislocations rather than dislocations of the DSG type.

In the next section we review briefly the DSG model, outline its salient features, and establish the relevant parameters which are used to impose conditions on the potentials employed in the MD simulations. In Sec. III, we present a detailed description of the procedures and criteria followed in selecting and calculating the interatomic potentials. We also detail the simulation procedure used in obtaining the relaxed reconstructed configuration employed in the MD experiments. The results from the MD experiments are presented in Sec. IV. We discuss the morphology of the relaxed configuration and compare some of its features with HAS (Ref. 4) and STM experiments[10] and present the calculated phonon dispersion curves along the ⟨110⟩ direction. Finally, we collect our comments and concluding remarks in Sec. V.

II. THE DOUBLE-SINE-GORDON MODEL AND ITS RELEVANCE TO THE RECONSTRUCTED PHASE OF Au(111)

A. The double-sine-Gordon model

The one-dimensional DSG model Hamiltonian can be written as

$$H=\int dx\left[\left[\frac{\partial\phi(x,t)}{\partial t}\right]^2+\frac{\mu}{2}\left[\frac{\partial\phi(x,t)}{\partial x}\right]^2+\frac{W_0}{2}\tanh^2(R_0)V(\phi)\right], \tag{2.1}$$

where $\phi(x,t)$ may be considered as a strain field; the first term represents the kientic energy of the system and the second term the elastic energy, where μ is the stiffness constant of the medium. $V(\phi)$ is an underlying potential and it can be expressed in the following form

$$V(\phi)=\left[\frac{4}{\cosh^2(R_0)}[1-\cos(\phi/2)]+\tanh^2(R_0)[1-\cos(\phi)]\right], \tag{2.2}$$

for the sake of simplifying the physical interpretation of the equilibrium solutions associated with the DSG Hamiltonian. The term $(W_0/2)\tanh^2(R_0)$ in (2.1) normalizes $V(\phi)$ to W_0. The DSG potential differs from its sine-Gordon counterpart in that it incorporates two harmonics of the field, which give rise to two types of minima in the potential.

The static-equilibrium solution for this system is obtained by deriving the Hamilton-Jacobi equations from the above Hamiltonian, and then setting the time-derivative terms to zero, giving

$$\frac{\partial^2\phi(x,t)}{\partial x^2}=\frac{1}{4l_0^2}\frac{\partial V(\phi)}{\partial\phi(x,t)} \tag{2.3}$$

with

$$l_0=\left[\frac{\mu}{2W_0\tanh^2(R_0)}\right]^{1/2}. \tag{2.4}$$

The solutions to this equation incorporate one or more DSG solitons depending on the boundary conditions imposed. The form of the DSG potential selected above allows expressing the DSG one-soliton solution as the sum of two sine-Gordon solitons centered at $X_0+l_0R_0/2\pi$ and $X_0-l_0R_0/2\pi$,

$$\phi(x)=\sigma_{\rm SG}\left[\frac{2\pi}{l_0}(x-X_0)+R_0\right]+\sigma_{\rm SG}\left[\frac{2\pi}{l_0}(x-X_0)-R_0\right], \tag{2.5}$$

where $\sigma_{\rm SG}(x)=(4/\pi)\tan^{-1}(e^x)$.

l_0 appears as a length scale for the soliton solution above, and X_0 is the position of its center of mass. The SG subsolitons are separated by a distance of $2R_0l_0/2\pi$, while the effective length of each subsoliton is $l_0/2$. The size of the DSG soliton, thus, depends on the parameters l_0 and R_0 that appear in the underlying potential. The DSG equation has been studied extensively in the literature.[28–32] One of the interesting features of this type of soliton is that it possesses an internal degree of freedom which has been compared to that of a diatomic molecule.[30]

A Frenkel-Kontorova-like DSG model is obtained from a discretized version of Hamiltonian (2.1). It represents the case of a one-dimensional chain of atoms connected by springs with spring constant μ and natural length b, and subject to a substrate potential similar to (2.2). The total potential energy of the chain is given by

$$V_N=\mu a^2\left[\tfrac{1}{2}\sum_{i=0}^{N-1}(u_{i+1}-u_i-p_0)^2+\frac{1}{4l_0^2}\sum_{i=0}^{N-1}\left[\frac{4}{\cosh^2(R_0)}[1-\cos(2\pi u_i)]+\tanh^2(R_0)[1-\cos(4\pi u_i)]\right]\right], \tag{2.6}$$

where a is the natural periodicity of the substrate potential. The strain field ϕ is replaced by a discrete variable $u_i=x_i/a$ ($\phi=4\pi u_i$), which represents the displacement of atom i from the ith absolute minimum of the underlying substrate potential $V_{\rm DSG}$, i.e., from the commensurate positions normalized to the substrate periodicity a. a now represents the unit of length in the system. Consequently, the length scale l_0 becomes

$$l_0=\left[\frac{\mu a^2}{2W_0\tanh^2(R_0)}\right]^{1/2}. \tag{2.7}$$

Finally, $p_0=1-b/a$ is the natural misfit between the chain and substrate periodicities. Minimization of (2.4) with respect to u_i yields the static discrete DSG equation

$$\Delta_i^2 u = \frac{\pi}{l_0^2}\left[\frac{2}{\cosh^2(R_0)}\sin(2\pi u_i)+\tanh^2(R_0)\sin(4\pi u_i)\right] . \tag{2.8}$$

$\Delta_i^2 u \equiv u_{i+1}-2u_i+u_{i-1}$ is the second difference of u_i.

For large l_0 values, the solution to (2.8) can be approximated by the continuum DSG soliton solutions. In the perspective of the Frenkel-Kontorova (FK) model the soliton solutions represent regions of departure from a periodic phase of the atom chain in registry with the underlying substrate potential; these departures can be regarded as localized defects termed misfit dislocations by Frank and van der Merwe.[26]

B. Relevance of the DSG model to the reconstruction of Au(111)

The structure of the reconstructed Au(111) surface has been interpreted as a two-dimensional lattice comprised of linear chains of double-sine-Gordon (DSG) dislocations oriented along the ⟨110⟩ direction, and stacked in a zig-zag pattern along the ⟨112⟩ direction. The details of this structural model and its fitting to He diffraction data have been worked out elsewhere.[9] In this section, however, we shall establish the similarities between the salient features of the substrate potential of the Au(111) and those of the DSG potential. Moreover, we shall demonstrate the relation of the parameters which appear in the DSG soliton solution to the energetics of the potential, and establish their relevance to the molecular-dynamics work presented in later sections.

The potential-energy minima at the surface are located at C sites (fcc stacking) and A sites (hcp stacking) (see Fig. 1). The two sites are not energetically degenerate when one type of stacking is favored. In fcc (111) surfaces the C sites should be favored if a continuation of the bulk occurs. In the case of the Au(111) surface, it has been proposed[19] that a redistribution of the sp electrons at the surface favors a reduction of the mean interatomic separation in the surface layer with respect to the bulk values. This reduction gives rise to a mismatch between the surface and atomic periodicities in the bulk. The creation of solitons or dislocations at the surface corresponds to a compromise between occupying the C sites and reducing the interatomic separation at the surface resulting in both fcc and hcp regions being present. The type of soliton is dictated by the energetics and topology of the underlying substrate potential. Figure 1 shows schematically the minimum-energy path which connects a C site with an A site. The bridge sites along the path $C\rightarrow A\rightarrow C$ correspond to saddle points in the three-dimensional substrate potential.

The substrate potential acting on the atoms of the Au(111) surface can be expanded in terms of the two-dimensional surface reciprocal-lattice vectors as

$$V(\mathbf{r})=\sum_{\mathbf{G}}[v_A(\mathbf{G})e^{i\mathbf{G}\cdot(\mathbf{r}-\delta)}+v_B(\mathbf{G})e^{i\mathbf{G}\cdot(\mathbf{r}+\delta)}] , \tag{2.9}$$

where $\{\mathbf{G}\}$ is the set of reciprocal-lattice vectors of the hexagonal (111) mesh and 2δ is the separation between the A and B sublattices. The coefficients $v_B(\mathbf{G})$ are greater than $v_A(\mathbf{G})$ if we assume that the interaction of the surface atoms with the A lattice is weaker than the corresponding interaction with the B lattice. Limiting the expansion to the shortest $\mathbf{G}$ vectors and restricting the path to $C\rightarrow A\rightarrow C$ we obtain

$$V(\rho)=2(2v_A-v_B)\left[\cos\left[\frac{2\pi}{d}\rho\right]\cos\left[\frac{2\pi}{3d}|\rho|\right]+\tfrac{1}{2}\cos\left[\frac{4\pi}{3d}|\rho|\right]\right] +2\sqrt{3}v_B\sin\left[\frac{2\pi}{3d}|\rho|\right]\left[\cos\left[\frac{2\pi}{d}\rho\right]-\cos\left[\frac{2\pi}{3d}|\rho|\right]\right] , \tag{2.10}$$

where $-d/2\le\rho\le d/2$ and we have parametrized the path by setting $\mathbf{r}=(x,y)=[\rho_1(1/\sqrt{3})(|\rho|-1)]$. d is the nearest-neighbor distance. $\rho=d/2$ and $-d/2$ corresponds to contiguous C sites, while $\rho=0$ puts us on the A site along the path: $V_C=-3(v_B+v_A)$ and $V_A=-3(v_B-2v_A)$, while at the bridge sites ($\rho=d/4$ and $-d/4$) $V_{Br}=-2v_B+v_A$.

one-dimensional double-sine-Gordon potential as long as the C and A sites are not energetically degenerate. The energy curve along this path can be written as

$$U_{CAC}(x)=E_C+V_{\mathrm{DSG}}(x) , \tag{2.11}$$

with

$$V_{\mathrm{DSG}}(x)=\frac{W_0}{2}\tanh^2(R_0)\left\{\frac{4}{\cosh^2(R_0)}\left[1-\cos\left[\frac{2\pi x}{d^*}\right]\right]+\tanh^2(R_0)\left[1-\cos\left[\frac{4\pi x}{d^*}\right]\right]\right\} . \tag{2.12}$$

The variable x represents the displacement along the path with a C site as the starting point, $d^*=(2/\sqrt{3})d$ is the length of the path, and W_0 is the peak-to-peak amplitude of the potential and is given by the energy difference between the bridge sites and the C sites: $W_0=E_{\mathrm{bridge}}-E_C$. The parameter R_0 depends on the ratio of the energy at the A sites to the energy at the bridge sites measured with respect to the energy at the C sites:

$$\frac{4\tanh^2(R_0)}{\cosh^2(R_0)}=\frac{E_A-E_C}{W_0}=\frac{3v_A}{v_B+4v_A} . \tag{2.13}$$

The values of the DSG parameters l_0 and R_0 are determined from the observed size of the dislocations in STM measurements[10] and from fitting the diffraction pattern to experimental He-scattering results.[9] From STM measurements the ratio of the size of A regions to C regions is approximately $\frac{1}{2}$. In terms of DSG parameters the size of the A regions is given by the separation between the SG subsolitons,

$$L_A=\frac{l_0R_0}{\pi} , \tag{2.14}$$

while the size of the C regions is given by

$$L_C=\Delta X-\frac{l_0R_0}{\pi} . \tag{2.15}$$

ΔX above is the separation between the centers of contiguous DSG dislocations. This separation can be equated to the size of the reconstructed unit cell along the $\langle 110\rangle$ direction. Using this and the observed ratio between A and C regions, one obtains a relation for the parameters l_0 and R_0,

$$l_0R_0\simeq 24 . \tag{2.16}$$

This relation, together with a previous fit to the diffraction pattern,[9] establishes the value of the DSG parameters which appear in the DSG solution (2.5): $l_0\simeq 8d$ and $R_0\simeq 3$ (d is nearest-neighbor separation in the bulk). The values of these parameters are introduced into Eqs. (2.7) and (2.13) to generate constraints in the potentials which describe the surface intralayer and interlayer interactions. It is these constraints which establish a direct connection between the type of surface interatomic interactions and the size of the observed reconstructed unit cell.

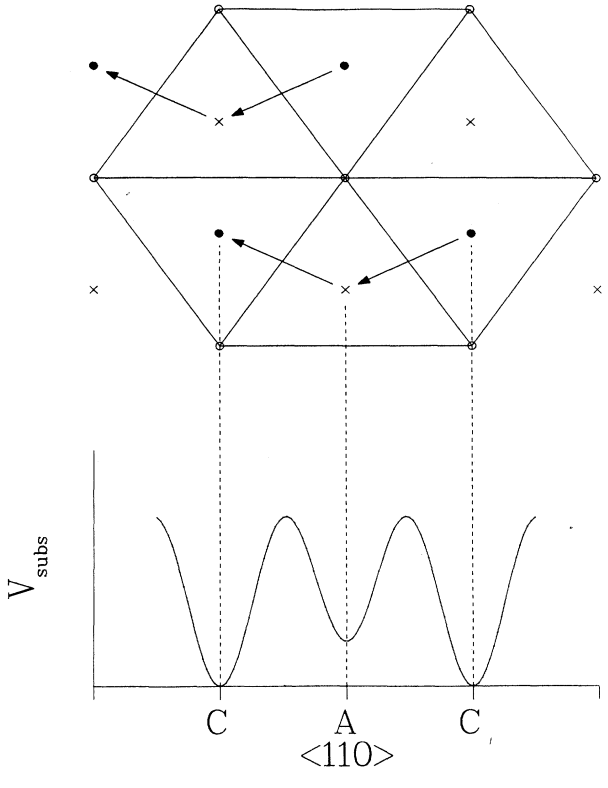

FIG. 1. Minimum-energy path of the surface reconstruction. The surface atoms occupy the C sites in the unreconstructed configuration: ●, C sites; ×, A sites; ○, B sites. Also shown is the profile of the substrate potential acting on a surface atom as it goes from a C position to an A position and back to a C position. The bridge sites correspond to the points along the path where it crosses the lines joining adjacent B atoms. These are points where the substrate potential is a maximum.

III. MOLECULAR DYNAMICS: MODEL AND METHODS

We compute the low-temperature small-amplitude surface-phonon dispersions of the reconstructed Au(111) surface along the $\langle 110\rangle$ direction using microcanonical molecular dynamics on slabs of various sizes. The forces on the slab particles are derived from an effective Hamiltonian

$$H=\sum_{i=1}^{N}\frac{p_i^2}{2M}+\tfrac{1}{2}\sum_{\substack{(i,j)\in S\\(j\neq i)}}V_{SS}(r_{ij}) +\tfrac{1}{2}\sum_{\substack{i\in S,\\ j\in B}}V_{SB}(r_{ij})+\tfrac{1}{2}\sum_{\substack{(i,j)\in B\\(j\neq i)}}V_{BB}(r_{ij}) . \tag{3.1}$$

The summation runs over an n-layer slab with N atoms and $r_{ij}=|\mathbf{r}_i-\mathbf{r}_j|$ is the distance between atom i and its jth neighbor. The bulk properties are assumed to be described by two-body potential V_{BB}. The interaction between two surface atoms is given by V_{SS}, while the interaction between a surface and a bulk atom is described by V_{SB}. We assumed radial forces and pairwise potentials. The choice of parameters for these potential is discussed in the next section.

A. Calculation of interatomic potentials

The criterion followed in calculating the potentials was based on several guiding factors which included the morphological properties of the reconstructed surface with the connection between the structural length scales and potential parameters established by the DSG model. Emphasis was placed in maintaining a physically simple picture and the ability to reproduce the salient features of the model with the least number of parameters. In principle, the functional form of the three potentials in (3.1) can be taken to be different; however, for the sake of simplicity, we took all three potentials to be of the same functional form. The form we adopted for the interatomic potentials was a Lennard-Jones (LJ) type truncated smoothly at a cutoff radius with the aid of a Gaussian function. This choice, although quite simple, reproduces the desired substrate potential curve with few parameters

(six, compared to 15 for the traditional polynomial or cubic spline type). The constraints imposed by the DSG model do not restrict the form of the bulk-bulk interaction. Assuming that the surface-bulk and bulk-bulk interactions could be treated the same as a first approximation, we have set the bulk-bulk potential equal to the surface-bulk potential with the only difference between the two being a multiplicative energy scaling factor. Although this approximation simplified the form of the effective Hamiltonian (3.1), it restricted the number of free parameters in the bulk-bulk potential to just one, the energy scale, which was adjusted by a best fit of the bulk-phonon dispersions. The potentials are written as

$$V_{SB}(r_{ij})=\varepsilon_{SB}U_B(r_{ij}) , \tag{3.2a}$$

$$V_{BB}(r_{ij})=\varepsilon_{BB}U_B(r_{ij}) , \tag{3.2b}$$

$$V_{SS}(r_{ij})=\varepsilon_{SS}U_S(r_{ij}) , \tag{3.2c}$$

with

$$U_B(r_{ij})=\left[\left[\frac{\sigma_B}{r_{ij}}\right]^{1/2}-\left[\frac{\sigma_B}{r_{ij}}\right]^{6} + A_B\exp[-s_B(r_{ij}-b_B)^2]+d_B\right] , \tag{3.3a}$$

$$U_S(r_{ij})=\left[\left[\frac{\sigma_S}{r_{ij}}\right]^{1/2}-\left[\frac{\sigma_S}{r_{ij}}\right]^{6} + A_A\exp[-s_S(r_{ij}-b_S)^2]+d_S\right] . \tag{3.3b}$$

The first step in the calculation is the generation of the substrate potential from the interatomic surface-bulk potential. The energy of interaction of individual surface atoms with the bulk atoms can be described as a function of distance by an interatomic potential curve. Assuming only central forces are present, the substrate potential at a position given by a vector $\mathbf{r}$ is equal to the sum of all the pairwise interactions between the atom at $\mathbf{r}$ and all its neighbors in the bulk,

$$V_{\text{subs}}(\mathbf{r})=\tfrac{1}{2}\sum_{j\in B}V_{SB}(|\mathbf{r}-\mathbf{r}_j|) . \tag{3.4}$$

The substrate energy curve along the path $C\rightarrow A\rightarrow C$ is generated by constraining $\mathbf{r}$ to vary along this path. A hard-sphere model was employed as a first approximation to obtain the variation in the Y and Z components of $\mathbf{r}$ as a function of its X component. Thus, starting with two contiguous C sites, the path connecting them can be described by a vector $\mathbf{r}=\mathbf{r}_0-\Delta\mathbf{r}$, where $\mathbf{r}_0$ references the position of the starting C site and $\Delta\mathbf{r}=(\Delta X,\Delta Y,\Delta Z)$, with ΔY and ΔZ given as a function of ΔX according to

$$\Delta Y=\frac{1}{\sqrt{3}}(\tfrac{1}{2}-|\tfrac{1}{2}-\Delta X|) , \tag{3.5a}$$

$$\Delta Z=(\tfrac{2}{3})^{1/2}-\left[\frac{3}{4}-\frac{(\frac{1}{2}-2\sqrt{3}\Delta Y)}{3}\right] , \tag{3.5b}$$

in units of the nearest-neighbor separation in the bulk. In the above equations $0\le\Delta X\le 1$. $\Delta X=\frac{1}{2}$ puts us on the A site, while $\Delta X=\frac{1}{4}$ and $\Delta X=\frac{3}{4}$ correspond to the bridge sites along the path. The DSG parameter R_0 is used to establish an energetic constraint on the substrate potential curve. This is done by requiring that the energy difference between A and C sites in V_{subs} be equal to that of the DSG potential curve (2.12) with $R_0\simeq 3.0$. Using (2.13) and writing W_0 as the energy difference between bridge and C sites we get

$$\frac{4\tanh^2(R_0)}{\cosh^2(R_0)}=\frac{V_{\text{subs}}(r_A)-V_{\text{subs}}(r_C)}{V_{\text{subs}}(r_B)-V_{\text{subs}}(r_C)} , \tag{3.6}$$

with V_{subs} given by (3.4). In order to have a finite value for the parameter R_0 above, V_{subs} has to distinguish energetically between A and C sites. This implies that V_{SB} must include at least third-neighbor contributions. In addition, V_{subs} and its derivative should be as smooth as possible in order to avoid the solitons from becoming *pinned* by spurious humps or discontinuities. We accomplish this by requiring U_B in (3.3a) and its first and second derivatives to go smoothly to zero at a truncation radius R_{TB}, which, as already indicated, must be greater than the separation between third neighbors. Finally, in order to ensure that the system would be stable at its nominal volume, we employed a stability condition derived by Johnson[33] which, neglecting volume forces, can be written as

$$\sum_{\substack{j\in B\\(j\neq i)}} r_{ij}\frac{\partial U_B(r_{ij})}{\partial r_{ij}}=0 , \tag{3.7}$$

where the sum is over all bulk atoms in a perfect fcc slab within a radius R_{TB} of atom i. We found that the parameter R_0 given by relation (3.6) varies slowly with the cutoff radius and with the location of the Gaussian function, which is specified by the parameter b_B in (3.3a). For a given radius, the parameter b_B is determined by employing (3.4) self-consistently with the other constraints. We set the cutoff radius for U_B, R_{TB}, equal to the fourth-neighbor separation. Using (3.4) together with

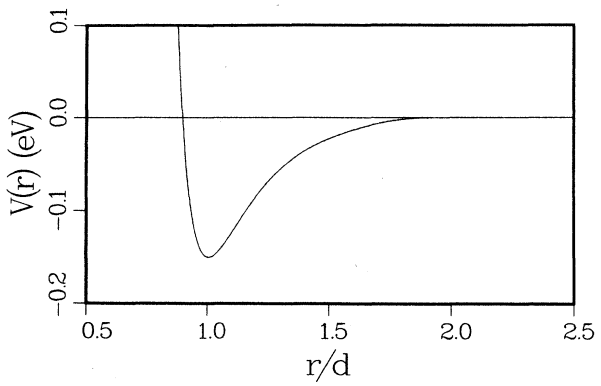

FIG. 2. Profile of the bulk-bulk potential. The interatomic distance is expressed in units of the nearest-neighbor separation $d=2.885$ Å.

(3.7) and the other truncation conditions, the parameters in v_B are determined uniquely.

The depth of V_{BB}, ε_{BB}, was adjusted by a best fit to experimental bulk-phonon dispersions. This parameter provided the energy scale of the other interatomic potentials. Figure 2 shows the bulk-bulk potential V_{BB} derived by using this prescription, and in Fig. 3 we show a comparison between bulk-phonon energies calculated using V_{BB} and neutron experimental data.[34] Finally, the only undetermined parameter left in V_{SB} is the depth of the potential ε_{SB}. The surface-bulk potential depth was adjusted relative to ε_{BB} to get a best fit of the surface shear-vertical phonon branch to experimental data. The fit amounted to reducing ε_{SB} by 20% relative to ε_{BB}. Figure 4 shows the substrate potential along the minimum-energy path $C \rightarrow A \rightarrow C$ calculated from V_{SB} using Eq. (3.4) together with the geometric constraints in (3.5). The dashed line corresponds to the DSG potential (2.12) with the parameter $R_0 = 2.96$. The difference in energy between the A and C sites is about 2.0 meV and the height of the bridge sites relative to the C sites is about 43.0 meV. It is important to mention that even though there is a difference in shape between the substrate potential (3.4) and the DSG potential (2.12), the DSG solution (2.5), through the definitions of the parameters R_0 and l_0, depends only on the height of the substrate potential (the bridge-site energy) and the difference in energy between A and C sites. The energy of both potentials in Fig. 4 agree at the bridge sites ($x = 0.25$ and 0.75), at the C sites ($x = 0$ and 1), and at the A sites ($x = 0.5$).

The parameters in the surface-surface potential V_{SS} are calculated employing a similar method. The strength of the potential is determined using Eq. (2.7), which establishes a connection between the length scale of the dislocations and the ratio of the force constant associated with the surface-surface interaction to the height of surface-bulk potential. Assuming that V_{SS} includes only first-neighbor contributions, we can write this relation from (2.7) as

$$l_0^2 = \frac{\partial^2 V_{SS}(r_{ij})}{\partial r_{ij}^2}\bigg|_{r_{ij}=R_S^0} (R_B^0)^2/2[V_{\text{subs}}(r_B) - V_{\text{subs}}(r_C)] \; . \tag{3.8}$$

The second derivative of V_{SS} is evaluated at R_S^0, which is the nearest-neighbor equilibrium separation of the unstrained surface layer in the absence of a substrate. R_B^0 is the nearest-neighbor separation in the bulk (substrate periodicity). Just as with U_B, additional constraints were imposed on U_S. Relation (3.8) is particularly simple in the case in which only nearest-neighbor interactions contribute. Assuming that the range of the surface intralayer potential can be taken to be shorter than the range of the bulk potentials, we truncated V_{SS} at a cutoff radius R_{TS} equal to the third-neighbor distance. Moreover, we imposed a value of zero for V_{SS} and for its first and second derivatives at R_{TS}. The equilibrium nearest-neighbor separation R_S^0 is determined by applying condition (3.7) to a mesh of atoms interacting via V_{SS},

$$\sum_{\substack{j \in S \\ (j \neq i)}} r_{ij} \frac{\partial U_S(r_{ij})}{\partial r_{ij}} = 0 \; . \tag{3.9}$$

where the sum is over all nearest neighbors of atom i in a two-dimensional mesh with the symmetry of the unrecon-

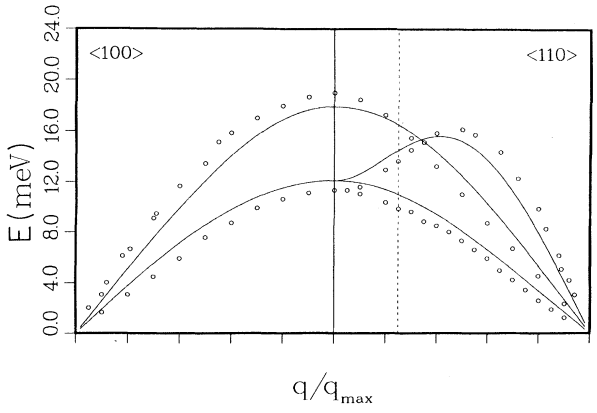

FIG. 3. Comparison between bulk-phonon-energy curves calculated using the bulk-bulk potential V_{BB} in this work and neutron-scattering data from Ref. 34.

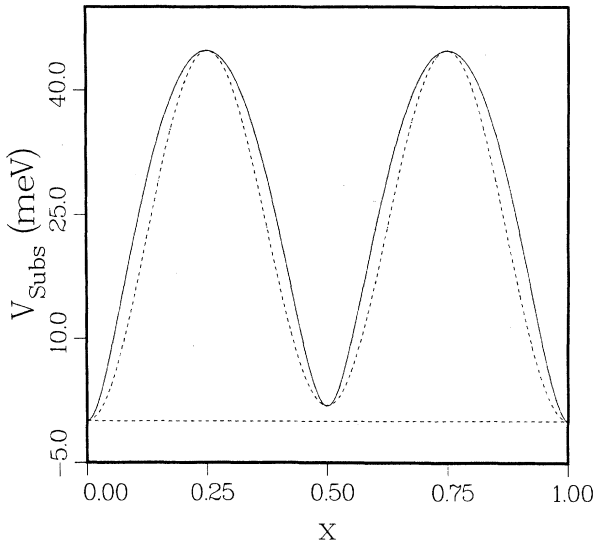

FIG. 4. Substrate potential profile (solid line) calculated from the surface-bulk interatomic potential V_{SB} using Eq. (3.4) and the kinematic constraints specified by Eqs. (3.5). The x axis refers to the $\langle 110 \rangle$ direction [ΔX variable in (3.5)]. The dashed line corresponds to the DSG potential (2.2) with $R_0 = 2.96$ and W_0 set equal to the energy difference between bridge and C sites given by (3.4). The energy difference between A and C sites is about 2 meV, while the height of the substrate potential at the bridge sites is close to 43 meV.

TABLE I. Parameters of the interatomic potentials used in the simulations. The form of the potentials is given in Eq. (3.2) and (3.3). $d=2.885$ Å is the nearest-neighbor separation in the bulk. p_0 is the mismatch introduced between surface-surface and surface-bulk interactions and is defined in Eq. (2.6).

$\varepsilon_{BB}=0.614\,11$ eV	$\varepsilon_{SS}=0.326\,00$ eV	$\varepsilon_{SB}=0.491\,29$ eV
$\sigma_B=0.911\,18d$	$\sigma_S=0.853\,78d$	$l_0=8.497\,28$
$s_B=21.113\,42/d^2$	$s_S=28.634\,89/d^2$	$R_0=2.957\,70$
$A_B=0.007\,26$	$A_S=0.015\,42$	$p_0=\frac{23}{24}$
$b_B=1.800\,00d$	$b_S=1.485\,42d$	
$d_B=0.005\,74$	$d_S=0.011\,73$	
$R_{TB}=2.000\,00d$	$R_{TS}=1.657\,92d$	

structed configuration. Finally, and more importantly, we introduced a misfit between the surface layer and the substrate by expressing the equilibrium nearest-neighbor distance of the unstrained surface layer R_S^0 as a rational fraction of the bulk nearest-neighbor distance R_B^0:

$$R_S^0/R_B^0=\tfrac{23}{24}\ . \tag{3.10}$$

This makes the surface-surface interaction attractive when the surface atoms occupy the substrate potential C minima which has a periodicity given by the nearest-neighbor separation in the bulk, R_B^0. The value of $\frac{23}{24}$ is dictated by the size of the reconstructed unit cell and the observed contraction of 4.4% along the $\langle 110\rangle$ direction. The misfit is isotropic since the potentials are spherically symmetric. However, it is energetically more favorable for the contraction to take place along the minimum-energy path $C\rightarrow A\rightarrow C$ indicated in Fig. 1. There are three such equivalent paths on a fcc (111) surface. In the present work we have looked at the case where the contraction takes place along only one of these paths. This restriction amounts to having all dislocations in the computational cell along the same direction. The values of the interatomic potential parameters calculated using the above prescription, together with the DSG parameters which result from employing conditions (3.4) and (3.8), are shown in Table I.

B. Simulation procedure

The study of the dynamics of the Au(111) surface reconstruction through molecular-dynamics simulations is computationally intensive due mainly to the large size of the reconstructed unit cell $[(22\pm1)\times\sqrt{3}]$ and to the large number of neighbors which contribute to the energy per atom, a consequence of the nondegeneracy between A and C sites. The long range of the potentials imposes conditions on the size of the computational cell, which has to be large enough so as to avoid atoms interacting with their own images once periodic boundary conditions are imposed. For the simulations, we take the computational cell to be a slab of n layers stacked in a fcc geometry with periodic boundary conditions along the $\langle 110\rangle$ direction (hereafter the X direction) and along the $\langle 112\rangle$ direction (hereafter the Y direction). The surface area of the MD cell must naturally be a multiple of the reconstructed surface unit cell. We take the size of the reconstructed unit cell to be $23\times\sqrt{3}$. Moreover, in order to avoid interactions of atoms with their images, the computational cell must be at least twice the size of the reconstructed surface unit cell along the Y direction. This makes the minimum XY size of each layer in the slab equal to $2\sqrt{3}\times23$ (in units of the nearest-neighbor distance in the bulk, $d=2.885$ Å). This is equivalent to four rows of atoms with 23 atoms per row in the bulk layers and 24 atoms per row in the reconstructed surface.

The slabs used in calculating the surface-phonon dispersions had 24 or 33 layers and one or two free surfaces, with one of them bulklike. Each layer had four or eight rows of atoms with 46 atoms per row in the bulk layers while the topmost layer had 48 atoms per row (two solitons along each row). The $T=0$ relaxed configuration was obtained by careful annealing and slow cooling the slab in a MD framework. An initial configuration is created prior to cooling by placing DSG solitons along the X direction on the topmost layer of an otherwise ideal fcc (111) n-layer slab. The atoms on each surface row are displaced from an initial commensurate position $\mathbf{r}_i^0=(X_i^0,Y_i^0,Z_i^0)$ to a new position $\mathbf{r}_i=(X_i,Y_i,Z_i)$ according to

$$X_i-X_i^0=-u_i=-\frac{1}{\pi}\left[\tan^{-1}\exp\left[\frac{2\pi}{l_0}(i-i_0)+R_0\right]+\tan^{-1}\exp\left[\frac{2\pi}{l_0}(i-i_0)-R_0\right]\right], \tag{3.11a}$$

$$Y_i-Y_i^0=f(u_i)=-\frac{1}{\sqrt{3}}\left(\tfrac{1}{2}-\left|\tfrac{1}{2}-u_i\right|\right), \tag{3.11b}$$

$$Z_i-Z_i^0=g(u_i)=\left[\tfrac{3}{4}-\frac{(\frac{1}{2}+2\sqrt{3}f(u_i)^2}{3}\right]^{1/2}-\left(\tfrac{2}{3}\right)^{1/2}, \tag{3.11c}$$

in units of the nearest-neighbor separation in the bulk. The displacement along the X direction follows the DSG solution (2.5), while the displacements along the Y and normal directions follow from geometric constraints which result from using a hard-sphere model.

The initial configuration one obtains employing this procedure, although close to the minimum-energy configuration of the slab, required careful annealing due to the ease in which the solitons can become trapped and due to the smallness of the Peierls-Nabarro (PN) potential[35] which arises because of the discreteness of the underlying substrate potential seen by the solitons. The minimum-energy configuration corresponds to the state in which all the DSG solitons lie at the bottom of the PN wells which have the periodicity of the underlying lattice. The depth of the PN wells is of the order of $\exp(-\pi l_0/2)$,[36,37] and is quite small due to the large value of l_0 associated with the dislocations. This makes it difficult to employ Monte Carlo methods of simulating annealing to find the minimum-energy configuration. The method we employed had three stages. In stage 1 we let the system relax by setting the kinetic energy of the particles in the slab to zero every time the total kinetic energy reaches a maximum. In stage 2 we input a small

amount of Gaussian noise into the velocities (of the order of 10^{-3} K) and let the system evolve for about 30 000 time steps (3.2×10^{-10} s) while monitoring the function[37]

$$\alpha(t)=\frac{1}{N}\sum_{i=1}^{N}\{[\mathbf{v}_i(t)]^2\}^2\Big/\left[\frac{1}{N}\sum_{i=1}^{N}[\mathbf{v}_i(t)]^2\right]^2 . \tag{3.12}$$

N above is the total number of particles in the slab. For a three-dimensional system this function fluctuates around $\frac{5}{3}$ when the system reaches thermal equilibrium, if the velocities obey a Maxwell distribution, with the fluctuations being of order $1/\sqrt{N}$. This soliton motion as it slides down the PN potential will increase the overall kinetic energy and will make $\alpha(t)$ peak when the solitons have maximum kinetic energy, which occurs at the bottom of the PN wells. The value of the function α at this point depends on the initial temperature. In our simulations it was found to be around 7–9 at the maximum. Figure 5 shows the function $\alpha(t)$ and the kinetic temperature of one of the presimulation runs as a function of time. The system reaches thermal equilibrium rather quickly and the average value of $\alpha(t)$ remains at $\frac{5}{3}$ for a while. The motion of the solitons is quite slow compared to the average atomic motion in the bulk, and one must look for a long time (compared to typical atomic times) in order to observe a change in $\alpha(t)$ due to the motion of the solitons towards a lower-energy state or to make sure that the system remains at thermal equilibrium for all times [i.e., $\alpha(t)=\frac{5}{3}$ for all observed times]. It should be noticed that although the sliding of the solitons to the bottom of the PN wells is identified easily by looking at the function $\alpha(t)$, the average atomic displacements which accompany this motion is small, of the order of 0.01–0.001 of the nearest-neighbor separation.

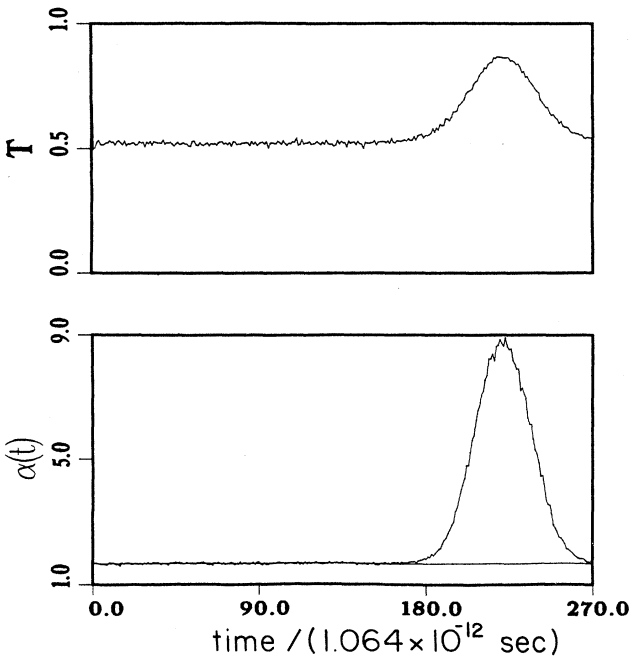

FIG. 5. Kinetic temperature (in reduced units) and function $\alpha(t)$ from Eq. (3.12) as a function of time for a presimulation run on a 24-layer slab. The time untis are in 1.064×10^{-12} s. The function $\alpha(t)$ remains constant at $\frac{5}{3}$ for a long time (about 18 000 time steps), indicating the system is in thermal equilibrium. The motion of the solitons towards a lower-energy state increases the particle velocities and the function $\alpha(t)$.

Finally, in stage 3 the kinetic energy of all the particles in the slab is set to zero when $\alpha(t)$ reaches its maximum. The configuration is then cooled using the same procedure employed in stage 1.

The approximate spectral distribution of the surface vibrations is calculated by taking the Fourier transform of the surface position-position correlation function,

$$g_{\alpha\alpha}(\mathbf{q},\omega)=\int dt\sum_n e^{i\omega t}e^{i\mathbf{q}\cdot\mathbf{R}_n}\langle u_n^{\alpha}(t)u_n^{\alpha}(0)\rangle \tag{3.13}$$

with $u_n^{\alpha}(t)=[R_n^{\alpha}(t)-R_{0_n}^{\alpha}]$; R_{0_n} is the equilibrium position of the nth particle. The angular brackets $\langle\ \rangle$ indicate averaging over equivalent rows [see Fig. 6(a)] in the MD cell and α is the polarization. The simulations were carried out at low temperature (10^{-6}–1 K). After allowing the system to thermalize, we let the system evolve at constant temperature for 25 000 MD steps (2.6×10^{-10} s), which are then used in the evaluation of (4.1). This gives a resolution to our phonon dispersions of about 0.016 meV. The equations were solved using a modified Euler method with two force evaluations per MD time step.

IV. RESULTS AND DISCUSSION

A. Surface structure

Figure 6(a) shows a top (XY) view of the top three layers of a 24-layer slab annealed according to the prescription described above. The surface unit has an extra atom per row compared to the bulk rows. The centers of the subkinks are located at the bridge sites (around atoms no. 8 and no. 17 in the bulk layers). The separation between the subkinks is a measure of the size of the hcp region of the reconstructed cell. From the figure we can see that is about 8.5 atomic spacings or about 24 Å. STM measurements[10] observe the atomic corrugation around the bridge sites as stripes which are interpreted as the domain boundaries between the fcc and hcp regions. The separation between these stripes is about 22 Å and the distance between pairs of stripes is about 44 Å.[10] This separation can be interpreted as the distance between subkinks belonging to different but contiguous DSG solitons. In the reconstructed configuration shown in Fig. 6(a) this separation is about 42 Å.

In the relaxed slab, the average interplanar distance is modified with respect to bulk values. The average outward relaxation decreases exponentially with layer number. Similarly, the corrugation of the surface due to the solitons propagates to other layers below the surface with the peak amplitude of the vertical corrugation decaying exponentially with layer number. Figure 6(b) shows the normal displacement of one row of atoms in each of the top three layers of a typical relaxed slab. The peak vertical amplitude at the surface is maximum around the

bridge sites with a value of about 0.2 Å. This is quite close to the corrugation height in STM pictures,[10] which is 0.15±0.04 Å. The vertical corrugation drops to 0.1 Å in the first layer below the surface, while it is about 0.08 Å in the second layer below the surface, as shown in Fig. 6(b).

In addition to vertical corrugation, the subsurface layers show a considerable amount of in-plane shear distortion. Figure 7 shows both X and Y distortions as well as normal corrugation as a function of layer number. Layer

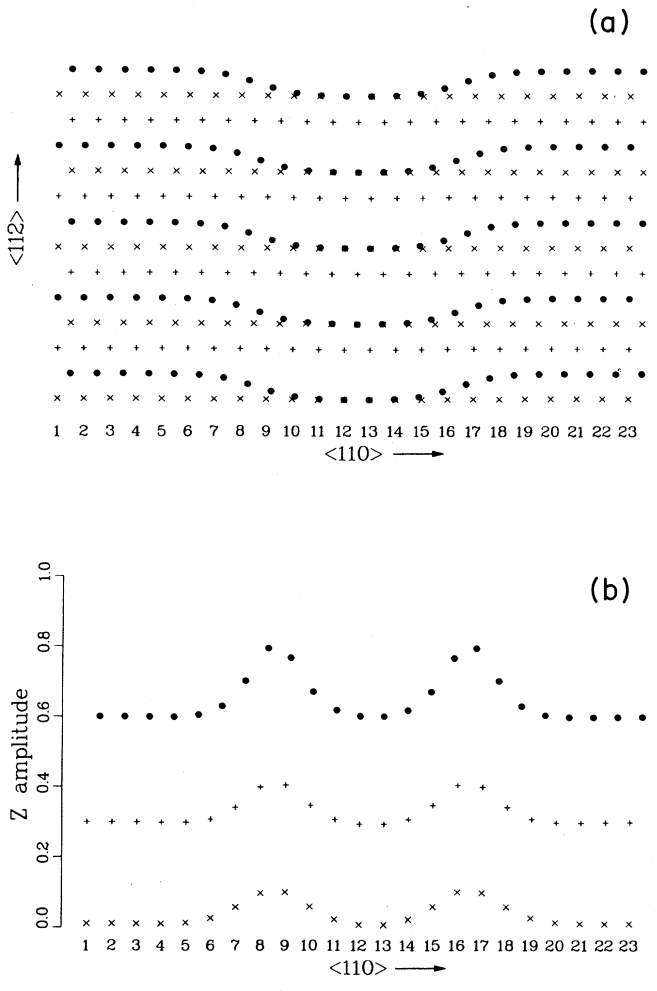

FIG. 6. (a) Planar view of the surface layer (●) of a 24-layer slab relaxed employing the procedure of Sec. III B. The atomic arrangement of the first layer below the surface (+) and the second layer below the surface (×) is also shown. The surface layer has an extra atom per row with respect to the bulk layers. (b) The normal corrugation of the first three layers (in Å) as a function of atom number: ●, surface atoms; +, first layer below the surface; ×, second layer below the surface. The corrugation is maximum around the center of the subsolitons. The separation between the layers is not related to the Z scale; however, the various layers are displaced with respect to each other for clarity.

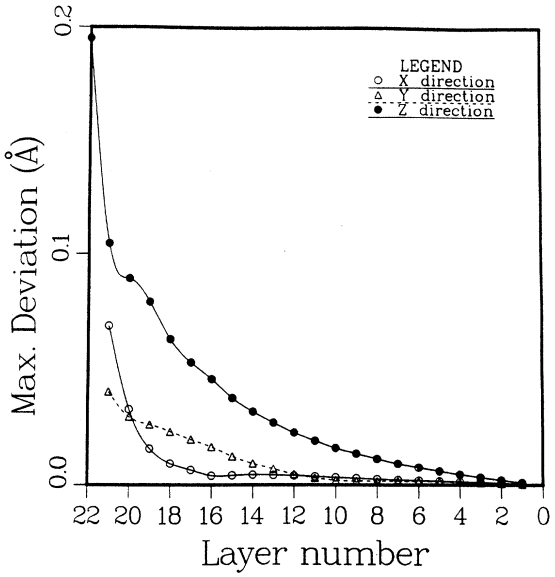

FIG. 7. Maximum distortion along the ⟨110⟩ (X), ⟨112⟩ (Y), and normal (Z) directions as a function of layer number. Layer 22 is the surface layer. The points plotted correspond to the atomic maximum deviation from the nominal value in each direction: ○, X; △, Y; ●, Z.

22 is the surface layer and the values plotted are the maximum deviations from the nominal unreconstructed value. The in-plane distortion decays faster than the vertical corrugation. Of all three, the distortion along the ⟨110⟩ direction decays fastest and becomes negligible after about six layers into the slab. On the other hand, the vertical corrugation decays slowly with layer number, although it changes quite rapidly in the first two layers below the surface. Similar anisotropy in the decay rates of atomic distortion has been observed in other MD studies of reconstructed Au surfaces which employ a different description of the interatomic potentials.[22–24]

B. Surface phonons and phasons

The surface-phonon dispersions are computed with $\mathbf{q}$ along the ⟨110⟩ direction. In contrast to the ⟨112⟩ direction the C_{3v} symmetry of the unreconstructed surface allows mixing of the three phonon polarizations along the ⟨110⟩ direction, which is due to the absence of reflection symmetry in the saggital plane. In fact, this lack of symmetry allows the observed reconstruction to take place. Furthermore, the symmetry of the reconstructed surface is C_1, which, together with the soliton superlattice, removes the degeneracies present at the K point of the unreconstructed SBZ.

For the sake of clarity we have plotted the dispersion curves for the three phonon polarizations separately. They are shown in Figs. 8(a)–8(c). Mode mixing is inferred by the overlap of points belonging to different polarizations, while the size of the points is proportional to their relative intensities. The lowest branch [Fig. 8(a)] shows a predominantly shear-vertical (SV) character (Z

polarization) from the $\bar{\Gamma}$ point up to about $\frac{3}{4}$ of the way to the $\bar{K}$ point. It becomes overdamped at wavelengths shorter than the width of the subsoliton domain walls (about four atomic spacings). This is due, partly, to the incommensurability of the domain-wall structure with the underlying strained substrate. This leads, in effect, to a crossover to quasilocalization where the phonon oscillations are confined to the A and C domains and are suppressed in the domain walls. The dispersion curve of the localized models is shifted up in energy to about 8

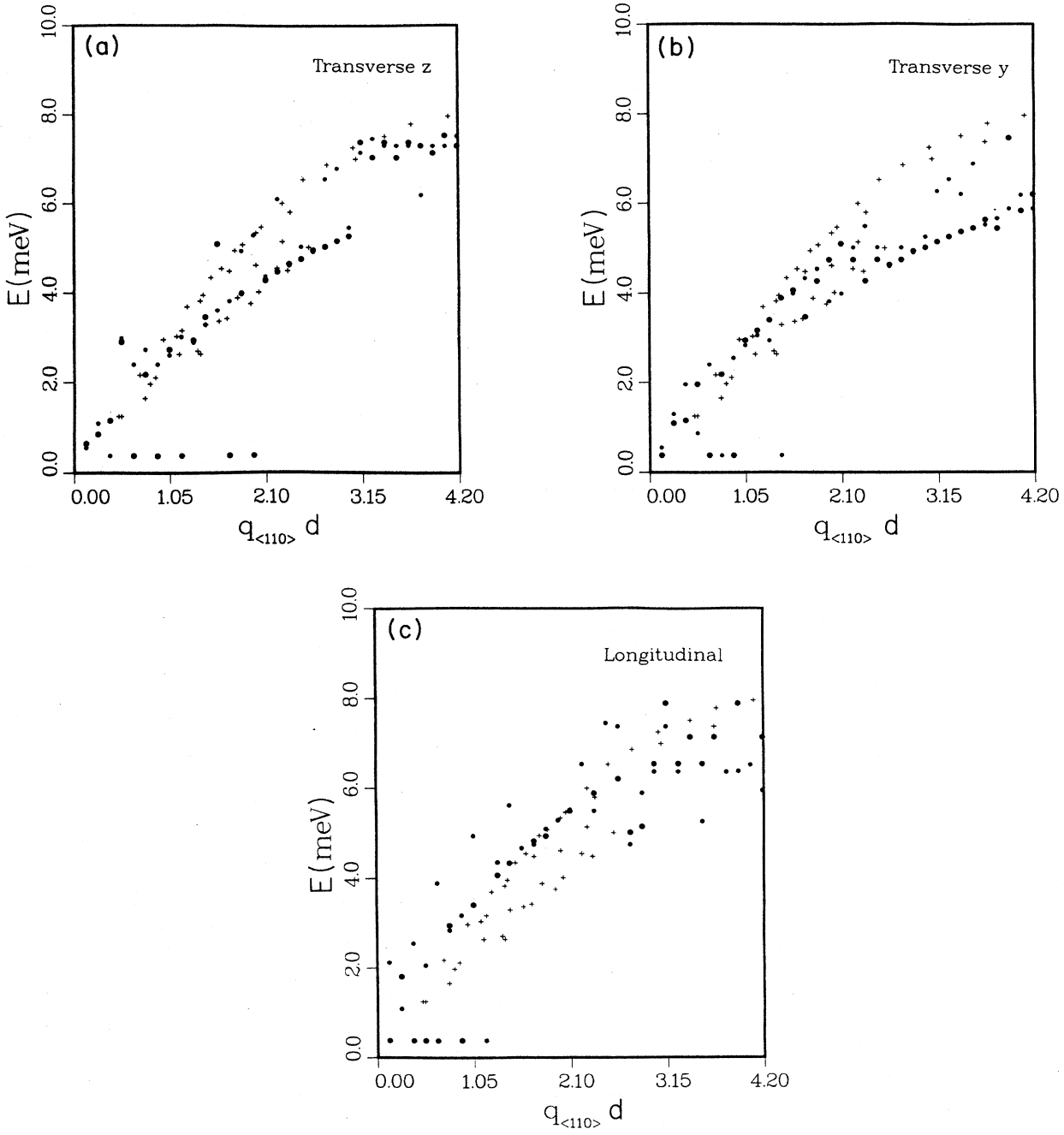

FIG. 8. Calculated surface excitations (solid dots) along the ⟨110⟩ direction together with experimental points (+) from Ref. 13. $d = 2.885$ Å is the nearest-neighbor separation. The size of the dots is proportional to the amplitude of the mode in q-ω space. Only the first two largest amplitudes at each discrete q value are shown. The three polarizations are plotted separately: (a) shear-vertical (transverse Z), (b) shear-horizontal (transverse Y), and (c) longitudinal (X). Phason modes appear in all three polarizations with the highest mode (about 0.4 meV) shown in these graphs.

meV, as can be seen in Fig. 8(a). The *A* and *C* modes are not degenerate. There is a small difference between the *A* and *C* phonon energies of about 0.016 meV. Superposition of Figs. 8(a) and (c) seems to indicate that this segment of the *SV* dispersion is a continuation of the highest phonon branch, which is predominantly of longitudinal character at smaller wave vectors as observed in Fig. 8(c).

The shear-horizontal (*SH*) polarization, which is inaccessible to HRHAS measurements, is predominant in the middle branch, Fig. 8(b), at long wavelengths. It exhibits

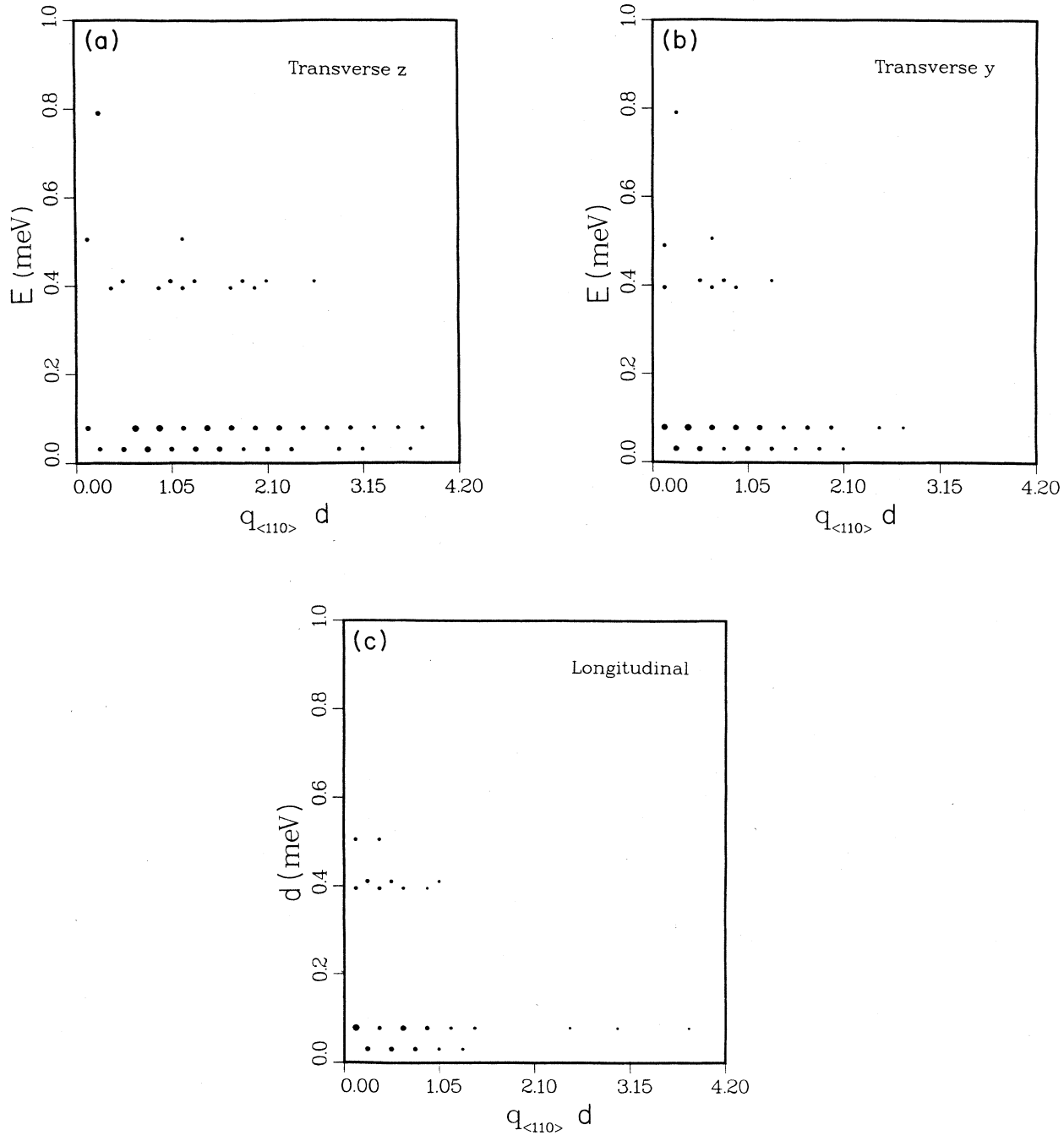

FIG. 9. Energy blow-up of the surface excitations along the ⟨110⟩ directions showing the phason branches. The three polarizations are shown separately. Only two points are seen for the acoustic and optical branches because the computational cell employed to calculate the modes had only two solitons along the ⟨110⟩ direction. The size of the dots is proportional to the amplitude of the mode: (a) transverse *Z*, (b) transverse *Y*, and (c) longitudinal.

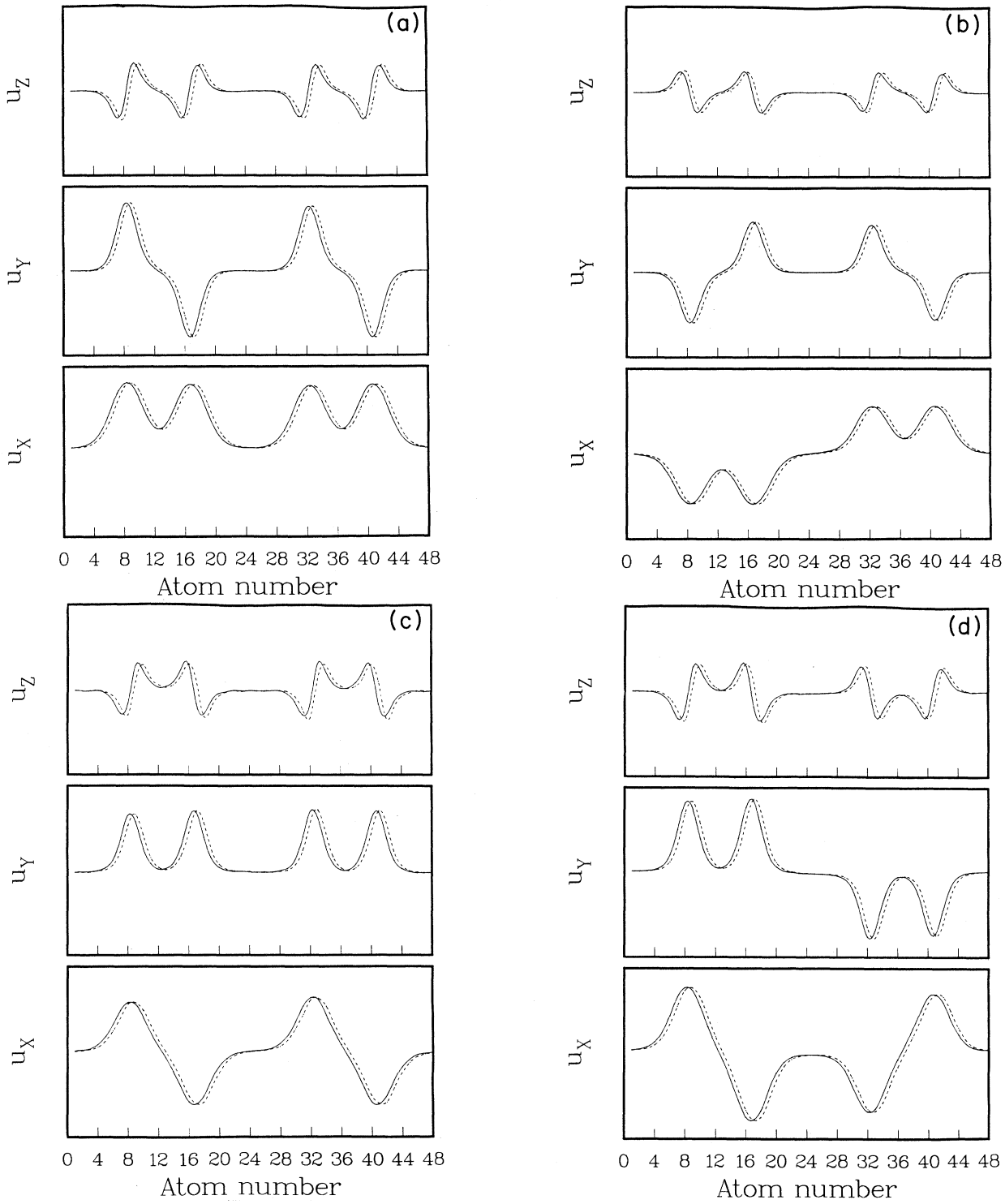

FIG. 10. Shape of the phason modes shown in Fig. 9. The four different modes which can be seen in that figure are shown separately. The modes are quasi-one-dimensional with the displacement along the X direction (u_x) given by one-dimensional DSG modes. The displacements along the Y and Z directions closely follow kinematic constraints (3.11b) and (3.11c) with u_i given by the shape of the mode along the X direction, u_X. The computational cell has two DSG solitons along each row. The dashed line corresponds to the second row in the surface unit cell. (a) Translational mode (energy $\simeq 0.03$ meV). Both solitons move in phase. (b) Acoustic-phason mode (energy $\simeq 0.08$ meV). Soliton centers move out of phase with respect to each other and internal oscillations are absent. (c) Lower point in the optical-phason branch ($\simeq 0.4$ meV). The internal mode of each DSG soliton is in phase with contiguous solitons. (d) Upper point in the optical-phason branch ($\simeq 0.41$ meV). The internal mode of each DSG soliton is out of phase with the internal mode of contiguous solitons.

a rather anomalous bifurcation about midway on the $\bar{\Gamma}$-$\bar{K}$ line The upper branch is just a continuation of the long-wavelength segment of the *SH* dispersion curve, while the lower branch overlaps with the end of the long-wavelength *SV* branch. The lower *SH* branch carries most of the oscillator strength of the *SH* polarization; however, it undergoes appreciable hybridization with longitudinal polarization close to the $\bar{K}$ point. Again, the splitting of the *SH* branch is associated with the stiffening of the domain-wall motion for wavelengths shorter than their width.

The experimental data are displayed as crosses in each of these figures for the sake of comparison. Bearing in mind the rather exclusive sensitivity of HRHAS to shear-vertical and long-wavelength longitudinal phonons, it is plausible to correlate the abrupt termination of the lower experimental phonon branch with an abrupt change in the character of the lowest branch from shear-vertical to shear-horizontal. Furthermore, the fact that the upper experimental branch can be traced to the SBZ edge can be attributed to the change of its character from longitudinal to vertical polarization at short wavelengths. HRHAS measurements of the anomalous longitudinal resonances in Cu, Ag, and Pt failed to trace this branch to the SBZ edge in spite of the fact that symmetry requires the presence of degeneracy between the *SH* and *L* modes at the $\bar{K}$ point.

Figure 9 is an expansion of the region below 1.0 meV of Fig. 8(a)–8(c). It shows two low-lying phason modes in all three polarizations. The flatness of these dispersion curves is a reflection of the fact that the MD computational cell contains two soliton superlattice periodicities along the $\langle 110 \rangle$ direction; consequently, only two points appear in each phason branch: one point at the superlattice BZ (SLBZ) center and the other at its edge. The flat dispersion curve is just an extended-zone representation of these two points.

The relaxed configuration, together with periodic boundary conditions, gives rise to an array of regularly spaced solitons or a soliton lattice with nonvanishing repulsion between contiguous DSG solitons. There are two types of phason excitations. The first of these derives from oscillations of the solitons about their mean positions. The dispersion relation for this type of excitation is the usual acoustic branch of a one-dimensional chain with nearest-neighbor interactions. The other type of excitation corresponds to oscillations of the subsolitons about the DSG center of mass. The modes associated with these oscillations are similar to the optical modes found in a one-dimensional chain with two different force constants; hence we label them "optical phasons." They arise in the DSG lattice because the interaction strength between subsolitons belonging to different DSG solitons is different (much weaker in the present case) from the interaction between the subsolitons in a given DSG kink. These phason modes are quite low in frequency due to the large value of the DSG parameters l_0 and R_0. The optical branch lies at about 0.4 meV, while the edge of the acoustic-phason branch terminates at about 0.08 meV. In spite of the long wavelength of the DSG phason modes ($\simeq 23d$), they are extremely localized in the surface region, where their amplitudes become negligibly small beyond the fourth subsurface layer. This is in clear contrast to the behavior of surface Rayleigh phonons whose penetration depth is comparable to their wavelength. As a consequence we find that the phason dispersion curves are rather insensitive to the thickness of slab as long as the number of layers exceeds about six.

A careful study of the eigenfunctions associated with these modes underlines the quasi-one-dimensional nature of the dislocations: the atomic displacements along the $\langle 110 \rangle$ direction are identical to the spatial eigenfunctions of the one-dimensional DSG model.[31] Furthermore, the atomic motion in the Y and Z directions follow closely the geometric constraints imposed by the functions f and g in (3.11). This can be seen by examining Figs. 10(a)–10(d), which show the atomic displacements in all three directions for the phason modes of Fig. 9. The spatial variation of u_Y and u_Z depends on the corresponding variation in u_X. This dependence can be approximated by the functions f and g in (3.11), where u_i is given by u_X. Figure 10(a) shows the lowest phason mode, at the SLBZ center, which depicts in-phase oscillation of the DSG soliton centers. The next mode, shown in Fig. 10(b), is at the SLBZ edge of the acoustic-phason branch. It involves out-of-phase motion of the centers of the solitons. Figures 10(c) and 10(d) show optical-phason modes at the SLBZ center and edge, respectively. Both of these modes involve the motion of the subsolitons about their center of mass.

The presence of these phason modes has not been reported in the HRHAS measurements. We attribute this to the resolution-limited sensitivity of HRHAS incapable of detecting such low-lying frequencies; however, a more careful analysis of the raw data might reveal their presence. Our MD study does not indicate any serious damping of these modes that might lead to a diffusive motion. It is also plausible that the technique of surface Rayleigh light scattering may be suitable to detect such long-wavelength modes, especially the optical phason.

V. CONCLUSION

We have studied the dynamics of the reconstructed surface of Au(111) in a molecular-dynamics formalism using the DSG model together with the morphology of the surface as the starting point for choosing constraints for the interatomic potentials. The agreement with the experimental phonon dispersions along the $\langle 110 \rangle$ direction is remarkable, given the very simple form chosen for the potentials appearing in the effective Hamiltonian (3.1). The substrate potential dictates the type of solitons favored in the reconstruction. The nondegeneracy between the A and C sites, which favors double-sine Gordon solitons, requires that the range of the surface-substrate potential includes at least third-neighbor contributions. We associate the difficulty of other models[24,27] in reproducing the right type of reconstructed unit cell with the limited range of the surface-substrate interatomic interaction assumed in these models. Moreover, the ratio of the energy difference between the A and C sites relative to the energy at the bridge sites is fixed by the

DSG soliton parameter R_0, which can be written in terms of the separation between the subsolitons or, more directly, in terms of the size of the A domains on the reconstructed surface. The structure and dynamics of the reconstructed surface are found to be quite insensitive to the fine details of the substrate potential, yet extremely dependent on the energetics of the A, C, and bridge sites.

All three surface-phonon branches show a strong amount of hybridization. We observed modes which seem to be localized at the A and C sites and with a Z polarization above a given q vector which can be related to the size of the subsolitons. The subsolitons become quite stiff at wavelengths shorter than their effective width and most of the motion is then concentrated away from these domain walls.

In the present work, the large softening of the longitudinal and shear-horizontal acoustic branches is introduced through relation (3.8), which establishes the length scale of the dislocations, and by the incorporation of misfit between the surface and the substrate, which induces a reduction of the surface-surface force constants. The misfit introduced is solely determined by the soliton density, which, in our model, was fixed to reproduce the superlattice periodicity of the reconstructed unit cell along the $\langle 110 \rangle$ direction. The spontaneous creation of solitons depends on the value of the misfit relative to the parameter l_0 which sets the length scale of the dislocations.[26]

Phenomenologically one would expect that the Cu(111) and Ag(111) surfaces also incorporate misfits with respect to the bulk. The fact that Cu(111) and Ag(111) surfaces do not reconstruct can be explained in this scheme by having the value of the misfit in these surfaces such that the system is stable against the spontaneous creation of solitons. The Cu, Ag, and Au(111) surfaces can be seen as systems in which the misfit progressively increases from Cu to Au and in the latter it reaches a critical value which energetically favors the spontaneous creation of dislocations. This critical misfit is not known for these surfaces.

The surface solitons are quasi-one-dimensional with the phason modes with polarization perpendicular to the solitons being described quite accurately by functions which follow from kinematic constraints imposed by a hard-sphere model. We can refer to these solitons as *soft* due to the almost absence of a gap in the phonon branch. A phason gap of about 3 meV is expected in the longitudinal-phonon dispersion if the soliton interacted with a hard substrate. The gap in this case corresponds to the mass of the solitons. Instead, we observed phonon modes as low as 0.5 meV in a slab made out of 33 layers. This might be an indication of small lock-in energies in the system.

Finally, at these low temperatures the solitons seem to be pinned by the Peierls-Nabarro potential. The frequency resolution in our simulations does not allow for a direct measure of the PN frequency. We can establish an upper bound with the PN frequency corresponding to energies smaller than 0.03 meV. However, the time scale for soliton diffusion can be quite longer than the time scales sampled in the simulations. Work on the finite-temperature properties of the system, as well as further investigation on the size of the phason gap together with the melting mechanism of the surface solitons, is currently in progress.

ACKNOWLEDGMENTS

We would like to thank Professor Charles Willis for extensive and useful discussions and the Boston University Information Technology Office for providing help in various stages of the programming. This work is supported by the U.S. Department of Energy under Contract No. DE-FG02-85ER45222.

[1]G. A. Somorgai, *Chemistry in Two Dimensions: Surfaces* (Cornell University Press, Ithaca, 1981).
[2]M. A. Van Hove, R. J. Koestner, P. C. Stair, J. P. Biberian, L. L. Kesmodel, I. Bartos, and G. A. Smorjai, Surf. Sci. **105**, 189 (1981).
[3]J. Perderau, J. P. Biberian, and G. E. Rhead, J. Phys. F **4**, 798 (1974).
[4]U. Harten, A. M. Lahee, J. P. Toennies, and Ch. Wöll, Phys. Rev. Lett. **54**, 2619 (1985).
[5]J. C. Heyraud and J. J. Metois, Surf. Sci. **100**, 519 (1980).
[6]Y. Tanishiro, H. Kanimori, K. Takayanagi, K. Yagi, and G. Honjo, Surf. Sci. **111**, 395 (1981).
[7]K. Takayanagi and K. Yagi, Trans. Jpn. Inst. Met. **24**, 337 (1983).
[8]P. G. Drazin, *Solitons* (Cambridge University Press, Cambridge, 1983).
[9]M. El-Batanouny, S. Burdick, K. M. Martini, and P. Stancioff, Phys. Rev. Lett. **58**, 2762 (1987).
[10]Ch. Wöll,, S. Chiang, R. J. Wilson, and P. H. Lippel, Phys. Rev. B **39**, 7988 (1989).
[11]P. Toennies, J. Vac. Sci. Technol. A **5**, 440 (1987).
[12]H. Ibak, J. Vac. Sci. Technol. A **5**, 419 (1987).
[13]W. Harten, J. P. Toennies, and Ch. Wöll, Faraday Discuss. Chem. Soc. **80**, 1 (1985).
[14]G. Armand, Solid State Commun. **48**, 261 (1983).
[15]J. E. Black, F. C. Shanes, and R. F. Wallis, Surf. Sci. **133**, 199 (1983).
[16]V. Bortolani, G. Santoro, U. Harten, and J. P. Toennies, Surf. Sci. **148**, 82 (1984).
[17]V. Bortolani, A. Francini, F. Nizzoli, and G. Santoro, Phys. Rev. Lett. **52**, 429 (1984).
[18]V. Bortolani, A. Francini, F. Nizzoli, and G. Santoro, Surf. Sci. **152/153**, 811 (1985).
[19]V. Heine and L. D. Marks, Surf. Sci. **165**, 65 (1986).
[20]C. S. Jahanthi, H. Bilz, W. Kress, and G. Benedek, Phys. Rev. Lett. **59**, 795 (1987).
[21]G. Santoro, A. Francini, V. Bortolani, U. Harten, and Ch. Wöll, Surf. Sci. **183**, 180 (1987).
[22]F. Ercolessi, M. Parrinello, and M. Tosatti, Surf. Sci. **177**, 314 (1986).
[23]M. Garofalo, E. Tosatti, and F. Ercolessi, Surf. Sci. **188**, 321 (1986).
[24]F. Ercolessi, A. Bartolini, M. Garofalo, M. Parrinello, and E. Tosatti, Surf. Sci. **189/190**, 636 (1987).
[25]P. Carnevalli, F. Ercolessi, and E. Tosatti, Surf. Sci. **189/190**, 645 (1987).

[26]F. C. Frank and J. H van der Merwe, Proc. R. Soc. London, Ser. A **200**, 125 (1949).
[27]Y. Okwamoto and K. H. Bennemann, Surf. Sci. **186**, 511 (1987).
[28]D. Campbell, M. Peyrard, and P. Sodano, Physica D **19**, 165 (1986), and references therein.
[29]P. Sodano, M. El-Batanouny, and C. Willis, Phys. Rev. B **34**, 4936 (1986), and references therein.
[30]S Burdick, M. El-Batanouny, and C. R. Willis, Phys. Rev. B **34**, 6575 (1986).
[31]C. R. Willis, M. El-Batanouny, S. Burdick, R. Boesch, and P. Sodano, Phys. Rev. B **35**, 3496 (1987).
[32]R. Ravelo, M. El-Batanouny, C. R. Willis, and P. Sodano, Phys. Rev. B **38**, 4817 (1988).
[33]R. A. Johnson, Phys. Rev. B **6**, 2094 (1972).
[34]J. W. Lynn, H. G. Smith, and R. W. Nicklow, Phys. Rev. B **8**, 3493 (1973).
[35]F. Nabarro, *Theory of Crystal Dislocations* (Clarendon, Oxford, 1967).
[36]C. Willis, M. El-Batanouny, and P. Stancioff, Phys. Rev. B **33**, 1904 (1986), and references therein.
[37]R. Boesch and C. R. Willis, Phys. Rev. B **39**, 361 (1989).
[38]W. Schommers, Z. Phys. **257**, 78 (1972).